Insights into reaction intermediates to predict synthetic pathways for shape-controlled metal nanocrystals

Michal Strach†[+], Valeria Mantella†[+], James R. Pankhurst†[+], Pranit Iyengar†, Anna Loiudice†, Shubhajit Das[§], Clémence Corminboeuf [§], Wouter van Beek[⊥], and Raffaella Buonsanti†*

† Laboratory of Nanochemistry for Energy (LNCE), Department of Chemical Sciences and Engineering, École Polytechnique Fédérale de Lausanne, CH-1950 Sion, Switzerland.

§ Laboratory for Computational Molecular Design (LCMD), Department of Chemical Sciences and Engineering, École Polytechnique Fédérale de Lausanne, CH-1015 Lausanne, Switzerland.

⊥ The Swiss-Norwegian Beamline (SNBL) - ESRF CS40220, 38043 Grenoble CEDEX 9, France.

[+] These authors contributed equally

[*] Corresponding author: raffaella.buonsanti@epfl.ch

ABSTRACT

Understanding nucleation phenomena is crucial across all branches of physical and natural sciences. Colloidal nanocrystals are among the most versatile and tunable synthetic nanomaterials. While huge steps have been made in their synthetic development, synthesis by design is still impeded by the lack of knowledge of reaction mechanisms. Here, we report on the investigation of the reaction intermediates in high temperature syntheses of copper nanocrystals by a variety of techniques, including X-ray absorption at a synchrotron source using a customized in-situ cell. We reveal unique insights into the chemical nature of the reaction intermediates and into their role in determining the final shape of the metal

nanocrystals. Overall, this study highlights the importance of understanding the chemistry behind nucleation as a key parameter to predict synthetic pathways for shape-controlled nanocrystals.

INTRODUCTION

Monodisperse metal nanocrystals (NCs) with well-defined size and shape continue to offer new opportunities in current materials research, spanning from catalysis to energy conversion and biomedicine.[1–4] Colloidal chemistry is a powerful synthetic tool to access NCs with a level of tunability which is superior to other techniques.[1–9] Often developed by a trial-and-error approach, synthetic routes commonly employ metal salts as precursors, organic ligands or surfactants to stabilize the intermediates and the final product, often a reducing agent, and a carrier solvent.[4–9] The final NC products are sensitive to several parameters, including temperature, atmosphere, reaction time, overall volume, as well as the time and rate of injection of additional reactants.[4–9] Despite the numerous reported procedures, the understanding of the reaction pathways, and how they relate to the NC size and shape remains limited. General guidelines and theoretical descriptions of reaction parameters/size/shape relations are reported in the literature.[4–9] In recent years, the development of in-situ techniques based on X-ray spectroscopy and electron microscopy has enabled progress in the understanding of NC formation.[10–45] However, most of these studies focus on low temperature syntheses in aqueous solution, which are easier to monitor without sophisticated in-situ set-ups. Furthermore, most of them describe the post-nucleation stage and aim at corroborating theoretical models for size control rather than for shape control. [10–45]

Here, we report an integrated approach to investigate the reaction intermediates during high temperature syntheses of shape-controlled Cu NCs. We chose Cu NCs as our model system for a number of reasons. They have been lately at the forefront of materials chemistry

research, especially due to their shape-dependent catalytic properties.[46–52] Additionally, Cu is included in a variety of promising multinary compounds (e.g. $CuInS_2$[53], Cu_3VS_4[54], copper vanadates[55], copper ferrites[56]); thus, understanding its chemistry is important in order to rationally develop the synthesis of these more complex systems as the next step. Unfortunately, the synthesis of Cu NCs is still in a primitive state compared to Au and Ag in terms of the variety of attainable shapes.[2,57] One of the underlying reasons for this is the difficulty in reducing Cu(II) or Cu(I) precursors and the susceptibility of Cu to oxidation when working in aqueous solution, which is the most common environment for the synthesis of noble metal NCs.[2,57] As a result of these challenges, Cu NCs have mostly been synthesized in organic solvents by us and by others.[49,52,58–61,62] Nevertheless, a rational strategy for synthesis design to produce them with controllable shapes is lacking. In this study, we focus on a set of reactions of copper bromide (CuBr) in oleylamine (OLAM), which form spheres or cubes in the presence of trioctylphospine (TOP) or trioctylphosphine oxide (TOPO), respectively.[52]

We investigate these syntheses by in-situ X-ray absorption spectroscopy (XAS) in a custom-made flask reactor combined with ex-situ techniques, which include Nuclear Magnetic Resonance (NMR) spectroscopy, mass spectrometry (MS), X-Ray Diffraction (XRD) and transmission electron microscopy (TEM). From the collected kinetic data, we correlate the chemical nature of the reaction intermediates to their conversion kinetics into Cu nuclei and eventually to the formation of Cu spheres and cubes. Thanks to these findings, we explain the formation of Cu octahedra occurring at a higher temperature and we learn how to modulate the reaction conditions in a predictive manner to obtain Cu tetrahedra, which have not been previously synthesized.

EXPERIMENTAL SECTION

Chemicals. Oleylamine (OLAM, technical grade, 70%), tri-n-octylphosphine (TOP, technical grade 90%), tri-n-octylphosphine oxide (TOPO, technical grade 90% and 99%) and copper(I) bromide (CuBr, 98%) were purchased from Sigma-Aldrich. Hexane (anhydrous, 95%) was purchased from TCI Deutschland GmbH and ethanol (anhydrous, 95%) was purchased from Acros. All of these chemicals were used as received without further purification.

Synthesis of shape-controlled Cu NCs.

Cu spheres: OLAM (35 mL) was introduced into a three-neck flask and kept under vacuum for 30 min. Then, CuBr (3 mmol) was added, and the flask was purged under N_2 for 15 min. Afterwards, the solution was heated to 80°C, and held at that temperature for 15 min. TOP (6 mmol) was injected into the flask; the temperature was then raised to 260°C with a heating ramp of around 10°C/min and maintained for 1 h (**Figure S1**, temperature profile). The solution was then cooled down by removing the heating mantle. The content of the flask was divided into 4 x 50 mL centrifuge tubes, around 30 mL of an ethanol/hexane mixture (1:2 v/v) was added to each of them and the product was collected by centrifugation at 5000 rpm for 10 minutes. After two dissolution/precipitation cycles, the NCs were suspended in anhydrous hexane for further analysis.

Cu cubes: OLAM (10 mL) and TOPO (25 mmol) were introduced into a three-neck flask and kept under vacuum for 30 min. Afterwards, CuBr (3 mmol) was added and the resulting solution was heated to 80°C; the temperature was maintained for 15 min. The temperature was then raised to 260°C with a heating ramp of around 10°C/min and maintained for 1 h (**Figure S1**, temperature profile). The solution was then cooled to 60°C by removing the heating mantle. The content of the flask was divided into 2 x 50 mL centrifuge tubes, around 25 mL of an ethanol/hexane mixture (1:2 v/v) was added to each of them and the product was

collected by centrifugation at 5000 rpm for 10 minutes. After two dissolution/precipitation cycles, the NCs were suspended in anhydrous hexane for further analysis.

As a side note, TOPO 90% and 99% are both suitable for the synthesis of nanocubes. The TOPO 99% leads to a higher reaction yield.

Cu octahedra: CuBr (2 mmol) was added to 4.48 mmol of TOP in a vial in a N_2 glove box and this solution was heated at 80°C for 1 h to form a Cu-TOP complex. In parallel, OLAM (20 mL) was degassed under dynamic vacuum at 80°C for 1 h in a three-neck flask, after which the temperature was raised to 335°C. Once the solvent temperature was stable, the Cu-TOP solution was rapidly injected and the mixture was stirred for 20 min at 335°C, during which the solution turned reddish-brown. After this time, the heating mantle was withdrawn to cool the mixture. The content of the flask was divided into 3 x 50 mL centrifuge tubes, 20 mL of an ethanol/hexane mixture (1:2 v/v) was added to each of them and the product was collected by centrifugation at 5000 rpm for 10 minutes. After two dissolution/precipitation cycles, the NCs were suspended in anhydrous hexane for further analysis.

Cu tetrahedra: CuBr (2 mmol), TOPO (4.48 mmol) and degassed OLAM (2 mL) were heated to 80°C in a vial under nitrogen for 1 h. In the meantime, OLAM (18 mL) was degassed under dynamic vacuum at 80°C for 1 h in a three-neck flask, after which the temperature was raised to 300°C. Once the temperature was stable, the CuBr/TOPO/OLAM mixture was injected dropwise (0.8 mL/min) into the hot OLAM. The mixture was stirred for 20 min. After this time, the solution was cooled down naturally by removing the heating mantle. The content of the flask was divided into 3 x 50 mL centrifuge tubes, 20 mL of an ethanol/hexane mixture (1:2 v/v) was added to each of them and the product was collected by centrifugation at 5000 rpm for 10 minutes. After two dissolution/precipitation cycles, the NCs were suspended in anhydrous hexane for further analysis.

In-situ X-Ray Absorption Characterization. In-situ X-Ray Absorption Spectroscopy (XAS) measurements were performed at the Swiss-Norwegian beamlines BM31 at the European Synchrotron Radiation Facility (ESRF) in France. XAS data was acquired in transmission mode with 30 cm ionization chambers with appropriate gas fillings. All in-situ experiments were carried out using our custom cell. The flight path through the sample was adjusted between 5 and 20 mm, depending on the concentration of the reaction mixture, to optimize the XAS signal. Beam size was adjusted to cover the entire smaller window surface (Ø=5 mm) and the cell was aligned with XYZ and two rotational motions with respect to the beam path. XANES spectra were acquired continuously every 20 s. As an internal energy standard, a Cu foil was inserted between two ionization chambers downstream from the sample cell. As the position of Cu foil did not change over time all observed changes are the result of the samples' chemistry. The spectra were normalized using standard procedures using the presto-pronto software consisting of a full GUI program suitable for the analysis of large data sets. The references were prepared from commercially available powders co-ground with BN in ratios corresponding to 2.5 attenuation length for each material.

Ex-situ Characterization.

Matrix-Assisted Laser Desorption/Ionization Time-of-Flight Mass Spectrometry (MALDI-TOF-MS). MALDI-TOF-MS analysis was performed using a Microflex instrument (Bruker Daltonics, Bremen, Germany). The instrument was operated in both positive and negative linear ion modes and each spectrum was collected using an average of 500 laser shots. Samples were prepared under N_2 atmosphere by combining analyte mixtures with *trans*-2-[3-(4-*tert*-butylphenyl)-2-methyl-2-propenylidene]malononitrile (DCTB) and then drop-casting the mixture onto a MALDI sample plate.

Electrospray Ionization Mass Spectrometry (ESI-MS). ESI-MS measurements were performed on an QExactive HF Orbitrap-FT-MS instrument, (Thermo Fisher Scientific, Bremen, Germany) coupled to an automated chip-based nanoelectrospray device (Triversa Nanomate, Advion, Ithaca, USA). Electrospray ionization was conducted at a capillary voltage of 1.4 kV and nitrogen nanoflow of 0.15 psi. MS experiments were performed in the positive ion mode.

Nuclear Magnetic Resonance (NMR). All NMR spectra were recorded on a Bruker AVANCE III HD 400 spectrometer fitted with a 5 mm BBFOz probe, operating at 400.13 MHz for ^{1}H NMR spectra and 161.98 MHz for ^{31}P{^{1}H} NMR spectra. ^{1}H NMR chemical shifts were referenced internally to residual solvent resonances (d_6-benzene, δ_H = 7.16 ppm; d_8-toluene, δ_H = 7.09 ppm), calibrated against an external standard ($SiMe_4$, where δ_H = 0 ppm). DOSY ^{1}H NMR spectra were recorded by first measuring a 1D ^{1}H NMR spectrum and taking note of the center line of the spectrum, the sweep width, the number of scans (ns = 8), and the receiver gain. Using these same parameters, further 1D ^{1}H NMR spectra were recorded using 5% and 95% gradient strengths. Typically, using a gradient length of 1000 μs, recovery delay of 100 μs and a diffusion delay of 50 ms gave satisfactory signal intensities at 5% and 95% gradient strengths. 2D DOSY NMR spectra were then recorded from 128 points using a linear gradient-strength ramp between 5% and 95% gradient strengths. Diffusion coefficients were obtained from fitting DOSY NMR resonances using Bruker Topspin software.

Transmission Electron Microscopy (TEM). TEM images were recorded on an Analytical JEOL-2100F FETEM using a beam energy of 120 kV, equipped with a Gatan camera. Samples were prepared by depositing one drop of the hexane solution containing the nanoparticles on the surface of copper grids (Ted Pella, Inc.). Size statistics were performed using the software ImageJ and counting 200 particles per sample.

X-ray Diffractometry (XRD). XRD measurements were conducted on a BRUKER D8 Advance diffractometer with Cu Kα radiation equipped with a Bruker LynxEye one-dimensional energy dispersive detector. The diffractometer operated at 40 kV and 40 mA with a Cu Kα source with wavelength of λ = 1.54 Å. Samples were prepared by drop-casting nanoparticles on low background silicon holders, previously washed with isopropanol and acetone.

RESULTS AND DISCUSSION

In the synthesis of Cu spheres and cubes, CuBr is used as the Cu precursor and OLAM as the solvent and supposed reducing agent; TOP or TOPO are employed as the supposed shape-directing ligands, with TOP promoting the formation of Cu spheres and TOPO promoting the formation of Cu cubes. The reaction schemes along with the TEM images are reported in **Figure 1A**. The rendering of the custom-made cell is shown in **Figure 1B**. This cell mimics a typical laboratory three-neck round-bottom flask, where colloidal NC syntheses are usually performed. Compared to the only two previous studies using a similar set-up[16,38], the cell includes additional features, i.e. flight-path regulation and kapton windows. The latter provide this set-up with more flexibility in terms of extending the accessible X-ray energy range down to 5 keV, and thus it is not limited to hard and semi-hard X-rays.

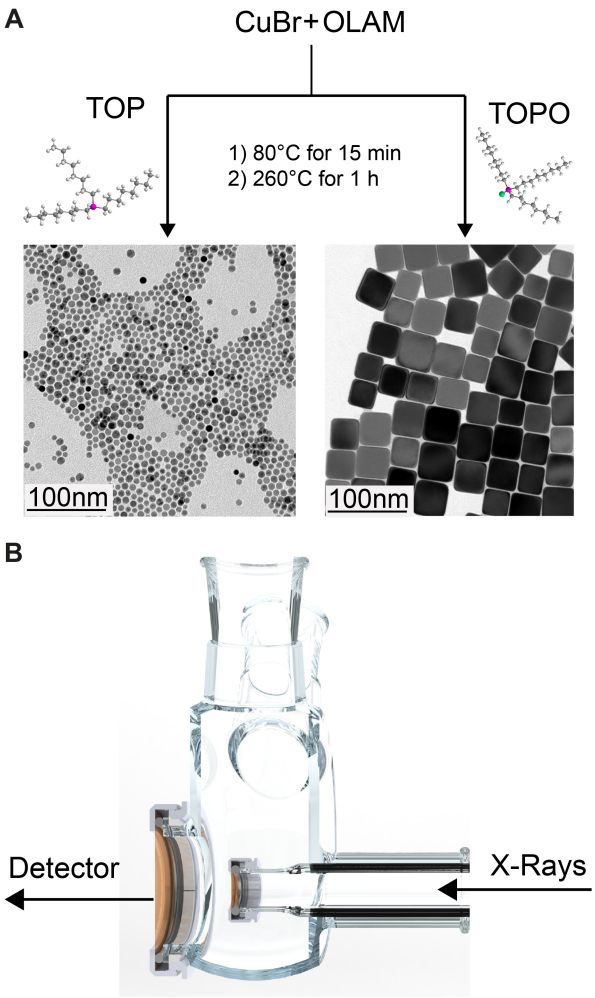

Figure 1. (A) Reaction scheme and representative TEM images of the Cu spheres and the Cu cubes studied in this work. (B) Rendering of the in-situ XAS reaction flask.

Below we discuss in-situ XAS measurements to monitor the compositional and structural changes during the three distinctive steps of the synthetic procedure (**Figure S1**): 1) the temperature plateau at 80°C; 2) the heating ramp from 80°C to 260°C; and 3) the temperature plateau at 260°C. We interpret these results in the context of formation of reaction intermediates and their conversion kinetics into Cu(0) nuclei, subsequently growing into Cu NCs. Finally, we correlate the conversion kinetics to the shape of the NC products.

Identification of the reaction intermediates.

In the synthesis of both cubic and spherical Cu NCs, the reaction mixture is heated at 80°C for 15 minutes before starting the temperature ramp to 260°C. The first goal was to understand the reactions of the Cu precursor (CuBr) during this stage. **Figure 2A** summarizes our findings; details of sample preparation and data fitting are reported in the Supporting Information. We found that CuBr forms the pseudo-tetrahedral $CuBr(OLAM)_3$ complex when dissolved in OLAM. Reaction of this complex with TOPO yields the monometallic, heteroleptic $CuBr(OLAM)_2(TOPO)$ complex through incomplete ligand exchange. In contrast, reaction with TOP completely substitutes all three OLAM ligands, yielding the bimetallic $\{CuBr(TOP)_2\}_2$ complex, where the two metal centers are bridged by μ_2-bromide ligands.

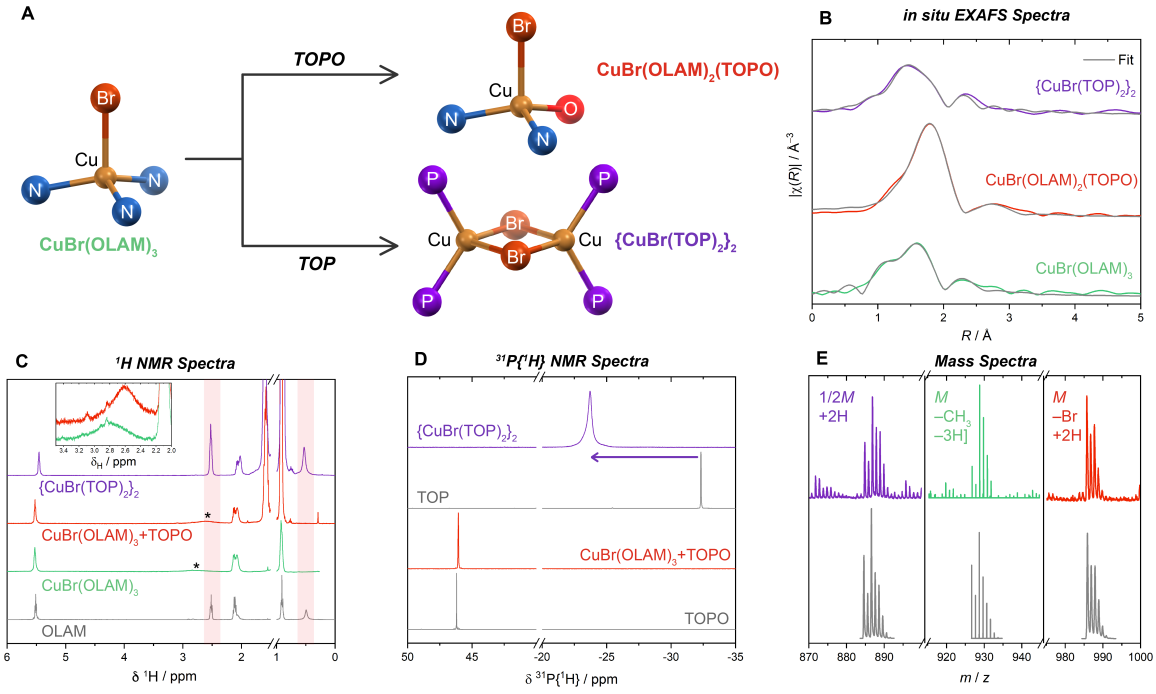

Figure 2. (A) Complexes formed at 80°C from reactions of $CuBr(OLAM)_3$ with TOPO and TOP, where TOP, TOPO and OLAM ligands are represented by their donor atoms P, O and N, respectively. (B) In-situ EXAFS spectra, all measured at the 80°C plateau. (C) ^1H NMR spectra of reaction mixtures after cooling from 80°C to room temperature; the spectrum

for OLAM is included for comparison. OLAM $C\underline{H_2}N\underline{H_2}$ resonances are highlighted in red, the broadened $C\underline{H_2}NH_2$ resonances are marked by * and shown separately in the inset plot. (D) $^{31}P\{^1H\}$ NMR spectra of TOPO- and TOP-containing mixtures, as well as the free ligands for comparison; the purple arrow highlights the shift of the phosphine upon coordination to Cu(I). (E) Mass spectra of reaction mixtures, measured by MALDI-ToF for TOPO and TOP complexes, and ESI-MS for the OLAM complex; *M* is the molecular ion, and the fragmentation or adduct formation required to give the simulated isotope patterns (gray) is indicated.

Using the in-situ reaction flask described above, we obtained the Extended X-Ray Absorption Fine Structure (EXAFS) spectra for the reaction mixtures during the 15-minute plateau at 80°C (**Figure 2B**). For the CuBr/OLAM mixture, the best fit of the data included one Cu–Br scattering path (r = 2.35 ± 0.05 Å) and three equivalent Cu–N paths (r = 1.97 ± 0.06 Å) (**Table S1**), thereby describing a pseudo-tetrahedral coordination geometry (**Figures S2**, **S3**). A shoulder in the EXAFS spectrum was accounted for by including a Cu···H close contact (r = 1.25 ± 0.03 Å), which could arise due to a nearby proton from an OLAM ligand. For the $CuBr(OLAM)_3$/TOPO mixture (**Figures S4, S5**), very poor fits were obtained using $CuBr(OLAM)_3$ or $CuBr(TOPO)_3$ models, and satisfactory fits were only obtained by using a mixture of Cu–O and Cu–N scattering paths in the model (r, Cu–O = 2.05 ± 0.04 Å) (**Table S2**). Whilst this indicates that the substitution of OLAM by TOPO does occur, it is incomplete at 80°C. Finally, the EXAFS spectrum that was measured after addition of TOP to the $CuBr(OLAM)_3$ solution was fitted using two Cu–P paths (r = 2.26 ± 0.04 Å) and two equivalent Cu–Br paths (r = 2.37 ± 0.02 Å) (**Tables S3, S4**), consistent with a halide-bridged bimetallic structure (**Figures S6- S8**).

A number of ex-situ measurements were carried out to further support these structures, (**Figures S9-S16** and **Table S5**). By ^{1}H NMR spectroscopy (**Figure 2C**), coordination of OLAM to the Cu(I) center in $CuBr(OLAM)_3$ was apparent from the disappearance of the amino-proton resonance (NH_2; 0.49 ppm for OLAM in d_6-benzene). Furthermore, the nearby methylene resonance (i.e. $C\underline{H}_2NH_2$; 2.52 ppm for OLAM in d_6-benzene) was severely broadened and also shifted by +0.27 ppm. Such broadening is expected upon coordination to the metal center, based on the quadrupolar moment of Cu that induces fast relaxation of nearby protons. Surprisingly, the room-temperature ^{1}H NMR spectrum of $CuBr(OLAM)_3$ was essentially unchanged in the mixture with TOPO, and no free OLAM was observed even with a four-times excess of TOPO present in the mixture. Considering that $CuBr(OLAM)_3$ gave a poor fit to the EXAFS data at 80°C, we suspect that there is an equilibrium between $CuBr(OLAM)_3$ and $CuBr(OLAM)_{3-x}(TOPO)_x$, where the former is preferred at low temperature and substitution by TOPO only occurs at higher temperature. In contrast, starker changes were observed in the ^{1}H NMR spectrum after addition of TOP to $CuBr(OLAM)_3$, where free OLAM was observed by the recovery of the amino- and methylene-protons at 0.49 and 2.52 ppm, respectively. All three OLAM ligands were completely substituted by only 2 equivalents of TOP, further supporting the $\{CuBr(TOP)_2\}_2$ formulation derived from the EXAFS spectrum (**Figure S8**).

Similar observations were made by $^{31}P\{^{1}H\}$ NMR spectroscopy, where the ^{31}P resonance for TOPO in the mixture with $CuBr(OLAM)_3$ was essentially unchanged in comparison with free TOPO (**Figure 2D**). In the case of TOP, the formation of $\{CuBr(TOP)_2\}_2$ induced a prominent shift in the ^{31}P resonance, such that the metal-phosphine resonance was observed at –22.1 ppm (–32.3 ppm for free TOP). Significant broadening of this resonance was also observed, again providing evidence for coordination to Cu(I).

Variable temperature NMR (**Figures S12, S14, S16**) and DFT calculations (**Table S6**) were in agreement with the substitution of OLAM by TOP being extremely favored even at room temperature while the substitution by TOPO possibly occurring only as the temperature raises.

Finally, molecular ion peaks were observed for all three of the proposed structures by mass spectrometry (**Figure 2E**): $[CuBr(OLAM)_3 - CH_3 - 2H]^+$ was found with an average mass at 929 *m*/*z* using electrospray ionization (ESI); $[CuBr(OLAM)_2(TOPO) - Br + 2H]^+$ was found at 987 *m*/*z* using matrix-assisted LASER desorption/ionization time-of-flight (MALDI-ToF); and one moiety of $\{CuBr(TOP)_2\}_2$ was observed using the same technique, i.e. $[CuBr(TOP)_2 + 2H]^+$, at 887 *m*/*z*.

Conversion kinetics of the reaction intermediates into Cu(0) nuclei.

After understanding the reactions occurring at the 80°C plateau, we performed in-situ XAS measurements during the next two steps of the synthesis procedure. Results for the heating ramp from 80°C to 260°C and for the 1 h plateau at 260°C are reported in **Figure 3** and **Figure 4**, respectively.

Figure 3A,B shows the X-Ray Absorption Near-Edge Structure (XANES) data acquired during the heating ramp. If one focuses on the Cu pre-edge feature, which is around 8982 eV, a progressive increase in intensity begins on commencing the heating ramp from 80°C both for the synthesis involving TOP (Figure 3A) and for the synthesis involving TOPO (Figure 3B).

To de-convolute the contributions of Cu(0), Cu(I) and Cu(II) to the Cu pre-edge, difference plots were extracted (**Figure S17**). From these, we plotted the intensities corresponding to the three Cu species normalized by the highest measured value, over time (**Figure 3C,D**). In the synthesis with TOP (**Figure 3C**), a faster increase of the Cu(0) signal

compared to Cu(I) and Cu(II) emerges during the ramp. Instead, when TOPO is used in the reaction (**Figure 3D**), the normalized intensities of Cu(0), Cu(I), Cu(II) follow the same kinetics during the heating ramp.

The simultaneous presence of the three Cu oxidation states in the XANES spectra suggests the occurrence of a disproportionation reaction in both syntheses. Experimental evidence of the disproportionation reaction is the color change from an initially pale yellow solution, containing the dissolved Cu(I) complexes, to red-brown upon formation of Cu(0). After centrifugation of the product, the remaining supernatant is light blue, which indicates the presence of Cu(II).

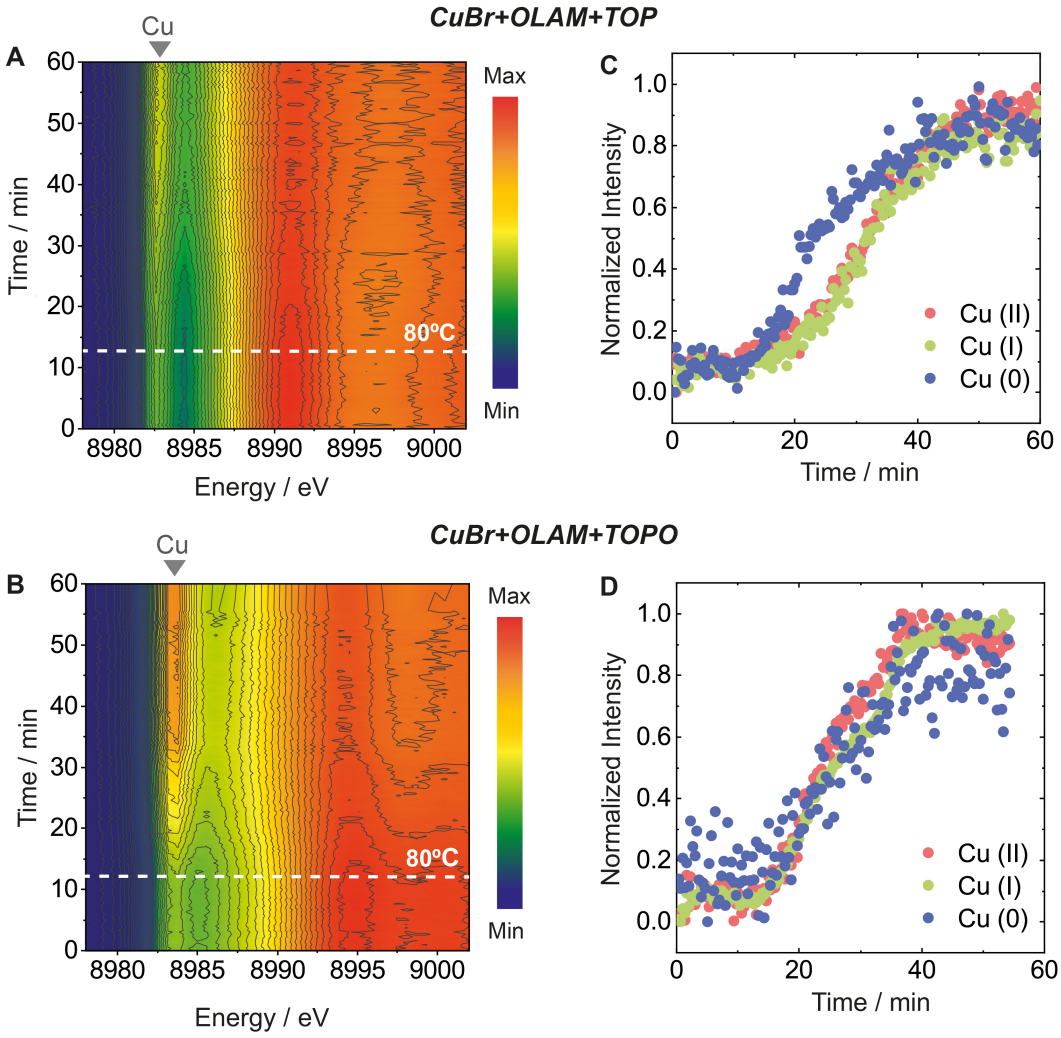

Figure 3. (A,B) Color maps of normalized XANES spectra collected during the heating ramp in the synthesis of Cu spheres and Cu cubes, respectively. (C,D) Intensities of the Cu(0), Cu(I), and Cu(II) pre-edges in the synthesis of Cu spheres and Cu cubes, respectively, normalized by the highest value observed during the ramp.

In a disproportionation reaction, we expect Cu(I) species to transform into equal quantities of Cu(0) and Cu(II). A certain equilibrium between the three species should be established at each temperature, being governed by the respective solvation energies, and corresponding to a fixed mass ratio. This behavior is exactly what we observe in the case of TOPO. Instead, in the case of TOP, the Cu(0) signal increases faster during the ramp compared to the other two species. To explain such a shift from the disproportionation equilibrium, we propose that the Cu(0) atoms assemble into stable Cu nuclei, thus no longer participating in the three-species equilibrium. Hence, we attribute the surge in the Cu(0) signal to the nucleation event. TEM on reaction aliquots corroborates this hypothesis as small Cu nanoparticles are observed starting at 150°C in the reaction with TOP (**Figure S18**). On the contrary, no to very little precipitate is collected during the heating ramp in the case of the reaction with TOPO. Here, small Cu nanoparticles are collected only when the temperature reaches 255°C (**Figures S19, S20**).

If now we turn to the data collected during the temperature plateau at 260°C (**Figure 4**), while the spectra cease to evolve in the TOP reaction, changes are visible for the TOPO reaction (**Figure 4A**). In particular, an increase of the Cu(0) signal and a concomitant decrease of the Cu(I) and Cu(II) signals are observed. To analyze the changes in more detail, we plot the intensities, normalized by the highest measured value, versus time (**Figure 4B**). It is evident that 10 minutes after the plateau is reached, a rapid increase of the Cu(0) signal

starts, which indicates a shift in the disproportionation equilibrium due to the formation of Cu(0) nuclei.

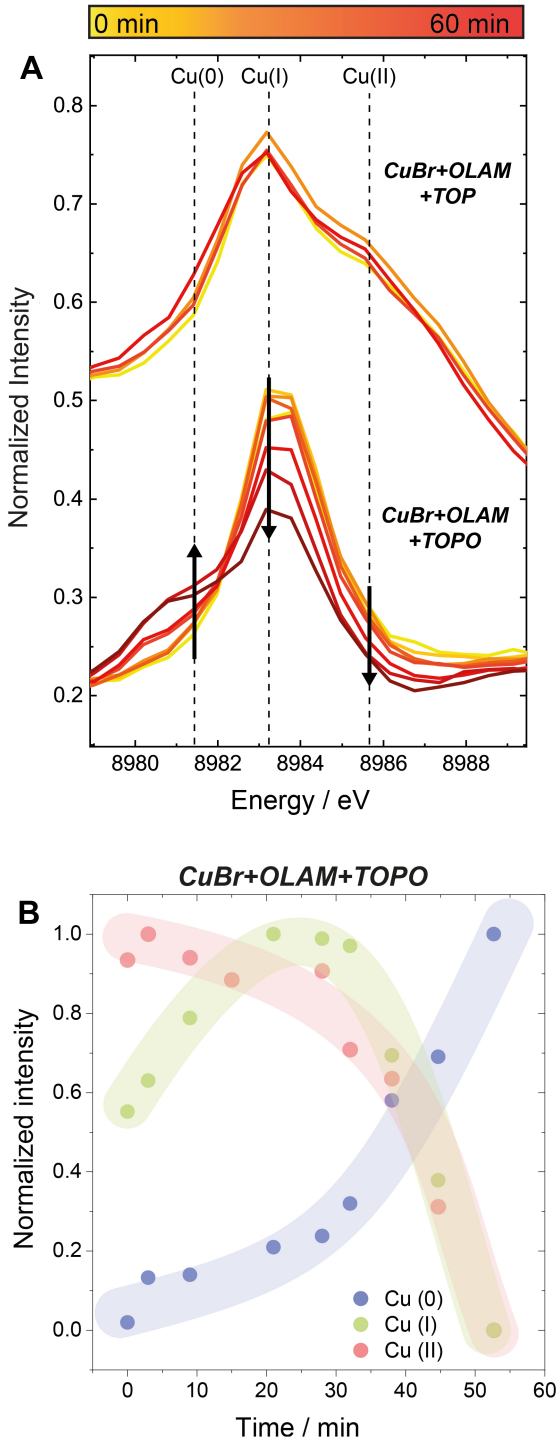

Figure 4. (A) Stack plots of the Cu K-edge spectra collected at the 260ºC plateau in the synthesis of Cu spheres and Cu cubes, respectively. (B) Intensities of the Cu(0), Cu(I), and Cu(II) pre-edges in the synthesis of Cu cubes, normalized by the highest value measured.

Based on all of the observations above, we propose that the nucleation event, manifesting itself as a shift in the disproportionation equilibrium, occurs during the ramp for the synthesis of Cu spheres with TOP and during the plateau at 260ºC for the synthesis of Cu cubes with TOPO. With knowledge of the nature of the initial Cu(I) intermediate complexes and the obtained kinetics data, we can now correlate the two and then discuss the impact of the reaction kinetics on the final NC shape.

Correlating the chemical nature of the reaction intermediates to their conversion kinetics.

The kinetic data from the in-situ XAS experiments reveal that the disproportionation of the TOP complex starts at lower temperature in comparison with the TOPO complex. In the TOP complex, the metal-ligand bond is stronger. However, since the two Cu(I) centers are pre-arranged in proximity of one another due to its bimetallic nature, the inner-sphere electron transfer and rearrangement of bromide ligands that occurs during disproportionation is expected to be favored (**Scheme 1**). For the monometallic TOPO complex, the metal-ligand bond is weaker. Yet, two equivalents of $CuBr(OLAM)_2(TOPO)$ must first approach one another and possibly associate in order for the electron transfer step to proceed (**Scheme 1**). DFT computations revealed that, despite the expected differences in metal-ligand bond strengths, the free energy of disproportionation is comparable for the two complexes (**Table S6**). Therefore, we must consider the kinetic implications of the Cu(I) intermediate structures, which emerge from the experimental evidences above, rather than the thermodynamics. We can rationalize the lower rate of disproportionation for the TOPO complex from the fact that two molecules are required for the reaction, and that during the heating ramp, there is a low equilibrium concentration of the Cu(I)-TOPO complex. An appreciable amount of Cu(I)-

TOPO is only obtained at high temperature, which is where we observe its disproportionation.

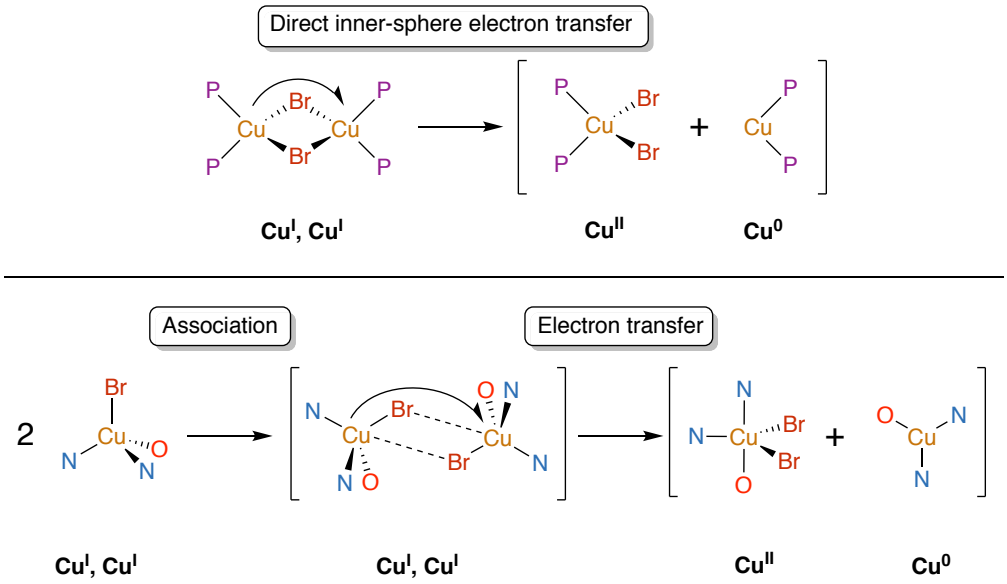

Scheme 1. Summary of the disproportionation pathways of $\{CuBr(TOP)_2\}_2$ and $CuBr(OLAM)_2(TOPO)$ complexes, where TOP, TOPO and OLAM ligands are represented by their donor atoms P, O and N, respectively. Oxidation states for Cu in each step are given. Square brackets indicate possible intermediate species that are expected to undergo rapid conversion to more stable forms (i.e. Cu(0) nuclei).

In addition to the disproportionation of the Cu-TOP and Cu-TOPO complexes, direct reduction of the CuBr percursor to Cu(0) nuclei should be considered. The strength of the reducing agent is an important parameter in low temperature syntheses of metallic nanocrystals.[3,32] Specifically, strong reducing agents usually result in the formation of NCs with equilibrium shapes. [3,32] Instead, milder reducing agents drive the reaction under kinetic control.[3,32] In our system, TOPO is not a reducing agent and TOP is unlikely to reduce metals in the absence of any oxygen source.[63] OLAM is the most plausible reducing agent and, moreover, it is present in large excess compared to TOP and TOPO in both Cu NC syntheses.

Therefore, the direct reduction of CuBr by OLAM, if any, would contribute to the generation of Cu(0) during the synthesis of Cu spheres and of Cu cubes equally.

Impact of the conversion kinetics on the Cu NC shape.

It is well established that precise control over NC shape can be accomplished by manipulating the reaction conditions (e.g. temperature, capping agents, precursor concentration). Depending on the chosen synthetic parameters, syntheses can be conducted under thermodynamic or kinetic regimes, giving access to NCs with different shapes.[3–9] More precisely, if a synthesis is thermodynamically driven, the NC will assume its equilibrium shape corresponding to the global minimum in Gibbs free energy, whereas, if a synthesis is kinetically driven, the NC will assume different shapes corresponding to local minima.[7] The competition between thermodynamic and kinetic products can be directed by varying the temperature and the monomer flux.[3–9] In particular, high temperature and/or low monomer flux favor the thermodynamic regime, while low temperature and/or high monomer flux lead to an end product dictated by the kinetic regime.[3–9]

For a fcc metal, such as Cu, the energetic sequence of the specific surface energies of the low-index crystallographic facets is $\gamma\{111\} < \gamma\{100\} < \gamma\{110\}$.[64] Based on this trend, the single crystal seeds should be thermodynamically stable as an octahedron where the {111} facets are all exposed on the surface. However, one should also consider that the NC will assume the shape which allows for the minimization of the total surface free energy. Because the resulting octahedron would possess a larger surface area than a cube of the same volume, the actual thermodynamically stable shape is a truncated octahedron enclosed by the {111} and {100} facets, which can be regarded as a quasi-sphere for smaller size particles.[2,7] Considering the above discussion, Cu NCs with other shapes (i.e. cubes, tetrahedra, etc.) will be kinetic products.

At this point, it remains to be defined what the monomers are. Across the literature, monomers are referred to as "the active species involved in the nucleation event".[3–9] The two common nucleation pathways to metallic NCs include 1) the aggregation of zero valent atoms and 2) the formation of multicenter cluster complexes by unreduced metal species prior to full reduction to the metallic state.[3,39] Ideally, EXAFS combined with X-Ray scattering and relative PDF analysis can help in catching the nucleation event and in identifying the actual monomer species.[39] Unfortunately, we could not perform such analyses during our syntheses because of the low concentrations of the involved species. Thus, we are unable to conclude as to whether 1) or 2) is the preferred nucleation pathway. Nevertheless, Cu(0) forms as a result of the disproportionation of the reaction intermediates. While recognizing that Cu(I) and Cu(II) intermediates can play a role in the nucleation step[65], we tentatively posit that Cu(0) forms the monomers in our system. Having established this, we can assume that the conversion kinetics of the reaction intermediates into Cu(0) are representative of the monomer flux.

With TOP, the shift in the disproportionation equilibrium (**Figure 3C**) suggests that a gradual flux of Cu(0) monomers is generated during the heating ramp from 80°C until the 260°C plateau; thus, the reaction is under thermodynamic control and quasi-spheres are ultimately achieved. Instead, in the case of TOPO, a sudden increase of Cu(0) occurs at the 260°C temperature plateau (**Figure 4C**). This high monomer flux in solution allows us to obtain kinetic products (i.e. cubes). Previous studies have reported selective binding of OLAM or Br^- to the (100) facets as being responsible of the final cubic shape.[60] Yet, we found no convincing evidence of the presence of OLAM or Br^- on the surface of the Cu NCs by XPS or FT-IR (**Figures S21-S22**). Furthermore, equivalent cubic or octahedral Cu NCs were obtained using CuCl as the Cu(I) source instead of CuBr (**Figure S23**).

Having correlated the conversion kinetics of the intermediates to the Cu(0) monomer flux and the final shape of the NC products, we decided to explore the free energy landscape of the reaction. The goal was to access other kinetic products, such as octahedra and tetrahedra. To the best of our knowledge, the latter have not been produced by any synthetic approach so far. To add more degrees of freedom in the reaction parameter space, we sought to investigate the monomer flux further through a series of reactions involving the injection of the pre-formed Cu complexes directly at high temperature (260ºC, 300ºC, 335ºC). The results are summarized in **Figure 5**. A rapid injection will induce a high flux, whereas a dropwise injection will lead to a lower monomer flux for the same reaction temperature. As the temperature raises, two phenomena occur. On one side, the conversion kinetics of the intermediates, and thus the monomer flux, are increased for the same injection modality, which favor a kinetic regime. Concomitantly, the rate of surface atom diffusion during the growth also increases, eventually favoring thermodynamically controlled products. These two opposite effects need to be considered when interpreting the results reported below.

The injection of the pre-formed $CuBr(OLAM)_2(TOPO)$ complex (obtained by reacting CuBr, OLAM and TOPO at 80ºC for 1 h) into OLAM at 260ºC induces a rapid color change to orange, which indicates the formation of Cu(0), and finally leads to the formation of nanocubes with truncated corners, both with a dropwise (0.8 mL/min) (**Figure 5A**) and with a rapid injection (within seconds) (**Figure 5B**). When the temperature is increased to 335ºC, spheres are isolated as the final product after dropwise injection (**Figure 5C**). Instead, nanocubes, though with smooth corners, are obtained with the rapid injection at this higher temperature (**Figure 5D**).

Interestingly, the injection of pre-formed $\{CuBr(TOP)_2\}_2$ (obtained by reacting CuBr and TOP at 80ºC for 1 h) into OLAM at 260ºC results in a subtle color change and produces spherical NCs both with a dropwise injection (**Figure 5E**) and with a rapid injection (**Figure**

5F), though in a very yield for the latter. When the temperature is increased at 335ºC, the dropwise injection leads to the formation of larger spheres (**Figure 5G**). Conversely, the rapid injection results in the formation of Cu octahedra as the final product (**Figure 5G, Figures S24-S26**). Independently from the temperature and the modality, the injection of the $\{CuBr(TOP)_2\}_2$ is always accompanied by a delayed color change of the reaction mixture (around 30 seconds for the rapid injection at 335ºC) from pale yellow to orange.

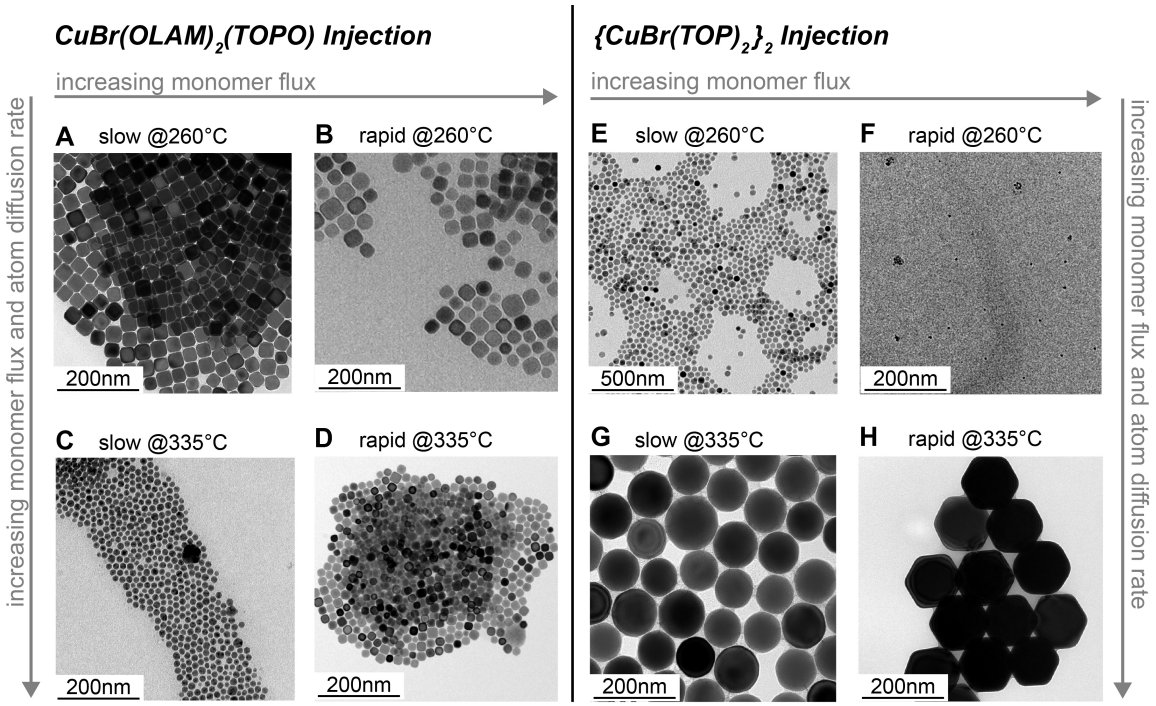

Figure 5. Representative TEM images of Cu NCs obtained after: (A,B) dropwise and rapid injection of $CuBr(OLAM)_2(TOPO)$ at 260°C, respectively; (C,D) dropwise and rapid injection of $CuBr(OLAM)_2(TOPO)$ at 335°C, respectively; (E,F) dropwise and rapid injection of $\{CuBr(TOP)_2\}_2$ at 260°C, respectively; (G,H) dropwise and rapid injection of $\{CuBr(TOP)_2\}_2$ at 335°C, respectively.

To explain these results, we have to consider that when preformed Cu-TOP and Cu-TOPO complexes are injected at high temperature, the rate of disproportionation is determined by

the associated thermodynamic barriers rather than their concentrations. The fact that the disproportion is slightly less endergonic for the Cu(I)-TOPO complex than the Cu(I)-TOP (**Table S6**) is in line with the experimental observation of slower conversion kinetics for the latter.

As indicated by the quick color change in solution, the $CuBr(OLAM)_2(TOPO)$ complex undergoes a very rapid disproportionation, resulting in a high monomer flux. A kinetic regime is established at 260ºC independently from the injection modality and cubes are obtained as the final product (**Figure 5A,B**). A rapid injection at 335ºC also leads to the formation of cubes (**Figure 5D**). Instead the combination of a dropwise injection, which lowers the flux, and higher temperature at 335ºC brings the system under thermodynamic control and quasi-spherical NCs are obtained (**Figure 5C**).

The higher free energy associated with the $\{CuBr(TOP)_2\}_2$ disproportionation lowers the overall Cu(0) monomer flux. Thus, the thermodynamically stable quasi-spheres are obtained at 260ºC, independent from the injection modality (**Figure 5E,F**), and at 335ºC with the dropwise injection **(Figure 5G)**. However, the rapid injection at 335°C allows the access to an intermediate regime where octahedral NCs are obtained (**Figure 5H**).

It is worth noting that the above discussion refers only to shape control, which is the focus of this study. Size variation among the NC products obtained in the different reactions can be explained by correlating the reaction conditions to the monomers consumed during the nucleation stage versus those remaining for the growth. As a general comment, bigger NCs can be obtained with the more slowly converting $\{CuBr(TOP)_2\}_2$ because less nuclei form, leaving more monomers available for the growth.

Finally, we predicted that by fine tuning the conditions that give octahedra, we could obtain shapes corresponding to other local minima. Indeed, carrying out a dropwise injection of the rapidly converting $CuBr(OLAM)_2(TOPO)$ at 300ºC resulted in tetrahedral Cu NCs

(**Figure 6, Figure S24**), which have not been previously reported. For a more reliable morphological analysis, the Cu tetrahedra NCs were tilted at different angles during TEM (**Figure S27**) and SEM images were also collected (**Figure S28**).

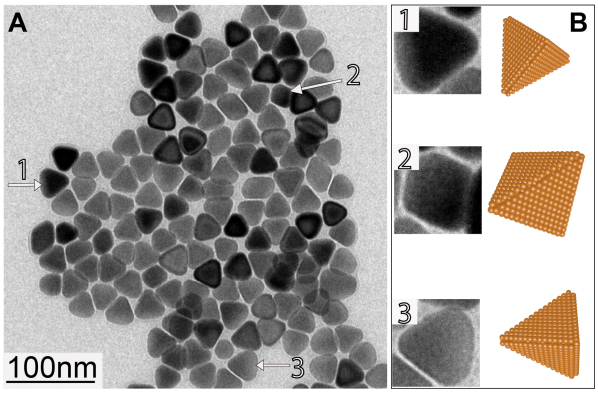

Figure 6. (A) Representative TEM image of Cu tetrahedra (33 ± 4 nm) obtained by dropwise injection of $CuBr(OLAM)_2(TOPO)$ into OLAM at 300°C. (B) TEM images and models of Cu tetrahedra in three common orientations, corresponding to those particles labeled with the same numbers in (A).

CONCLUSIONS

In conclusion, we have studied the colloidal synthesis of Cu NCs as one example of NC formation in organic solvents, using a variety of techniques including in-situ XAS in a custom-made reaction cell. Learning about the reaction kinetics was key in order to correlate the chemical nature of the identified reaction intermediates to the Cu(0) monomer flux, which in turn explains the shape of the final NC products. With follow-up experiments, we explored further the applicability of the acquired knowledge and uncovered a new synthetic route towards monodisperse Cu tetrahedra, a shape which had not yet been isolated. Based on these results, a correlation between the final Cu NC shape and the monomer flux can be finally established **(Figure 7**). With truncated octahedra, octahedra, cubes and tetrahedra, we have not yet exhausted the shapes achievable from single crystal seeds (**Figure S20**). Further

manipulation of the reaction conditions (i.e. a faster precursor injection, which represents a technical challenge at this moment) might provide access to additional Cu polyhedrons, such as rhombic dodecahedra.

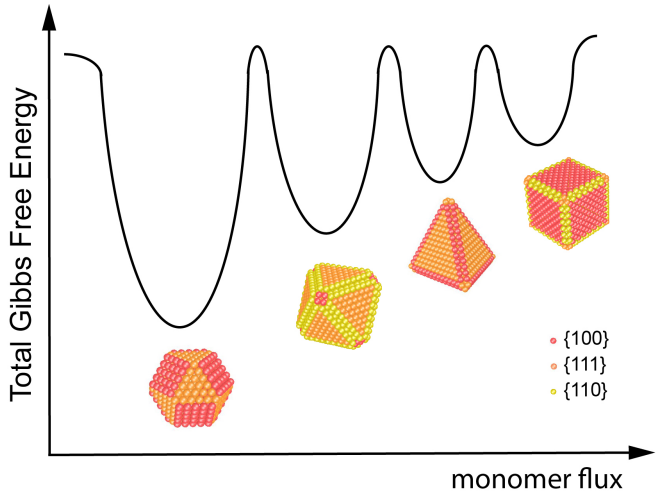

Figure 7. Schematic illustration of the free energy landscape for the Cu NC synthesis. The total Gibbs Free Energy is plotted versus the increasing monomer flux. A low flux of Cu (0) monomers generates the thermodynamically stable Cu quasi-spheres, which occupy the global energy minimum. Higher monomer fluxes provide access to other kinetic products which correspond to local minima. The relative Gibbs free energies are assumed based on the specific surface energies $\gamma\{111\} < \gamma\{100\} < \gamma\{110\}$.

As a general lesson on the synthesis of colloidal metal NCs, we have learned that the choice of the precursor and the identification of the reaction intermediates are crucial to enable a more rational approach to shape control.

ASSOCIATED CONTENT

Supporting Information. Information related to sample preparation, EXAFS fitting, NMR analysis, and additional TEM and XRD results. This material is available free of charge via the Internet at http://pubs.acs.org.

ACKNOWLEDGEMENT

This work was financially supported by the H2020 Marie Curie Individual Fellowship grant, agreement number 753124 for M.S., by the Swiss National Science Foundation (AP Energy Grant, project number PYAPP2_166897/1) for V.M., by the ERC Starting Grant -HYCAT with Agreement Number 715634 for J.R.P. and by Gaznat S.A. for P.I. C.C. and S.D. acknowledge the EPFL and the Swiss National Science Foundation (Grant No. 200020_175496) for financial support. The in-situ XAS experiments were performed on the Swiss-Norwegian beamline BM31 at the European Synchrotron Radiation Facility (ESRF), Grenoble, France (proposal numbers CH5233 and CH5586). Dr N. Gasilova is acknowledged for the mass spectrometry measurements. The authors thank Dr J. Huang for helpful discussions.

REFERENCES

(1) Kovalenko, M. V; Manna, L.; Cabot, A.; Hens, Z.; Talapin, D. V; Kagan, C. R.; Klimov, X. V. I.; Rogach, A. L.; Reiss, P.; Milliron, D. J.; et al. Prospects of Nanoscience with Nanocrystals. *ACS Nano* **2015**, *9*, 1012–1057.

(2) Yang, J.; Choi, M. K.; Kim, D. H.; Hyeon, T. Designed Assembly and Integration of Colloidal Nanocrystals for Device Applications. *Adv. Mater.* **2016**, *28*, 1176–1207.

(3) Xia, Y.; Xiong, Y.; Lim, B.; Skrabalak, S. E. Shape-Controlled Synthesis of Metal Nanocrystals: Simple Chemistry Meets Complex Physics? *Angew. Chemie Int. Ed.* **2009**, *48*, 60–103.

(4) Schaak, R. E.; Williams, M. E. Full Disclosure: The Practical Side of Nanoscale Total Synthesis. *ACS Nano* **2012**, *6*, 8492–8497.

(5) Kwon, S. G.; Hyeon, T. Formation Mechanisms of Uniform Nanocrystals via Hot-Injection and Heat-Up Methods. *Small* **2011**, *19*, 2685–2702.

(6) Lee, J.; Yang, J.; Kwon, S. G.; Hyeon, T. Nonclassical Nucleation and Growth of Inorganic Nanoparticles. *Nat. Rev. Mater.* **2016**, 1, 16034 – 16050.

(7) Xia, Y.; Xia, X.; Peng, H.-C. Shape-Controlled Synthesis of Colloidal Metal Nanocrystals: Thermodynamic versus Kinetic Products. *J. Am. Chem. Soc.* **2015**, *137*, 7947–7966.

(8) Gebauer, D.; Wolf, S. E. Designing Solid Materials from Their Solute State: A Shift in Paradigms toward a Holistic Approach in Functional Materials Chemistry. *J. Am. Chem. Soc.* **2019**, *141*, 4490 – 4504.

(9) Wang, F.; Richards, V. N.; Shields, S. P.; Buhro, W. E. Kinetics and Mechanisms of Aggregative Nanocrystal Growth. *Chem. Mater.* **2014**, 26, 5–21.

(10) Koziej, D. Revealing Complexity of Nanoparticle Synthesis in Solution by in Situ Hard X-Ray Spectroscopy - Today and Beyond. *Chem. Mater.* **2016**, *28*, 2478–2490.

(11) Jong Min Yuk, Jungwon Park, Peter Ercius, Kwanpyo Kim, D. J. H.; Michael F. Crommie, Jeong Yong Lee, A. Zettl, A. P. A. High-Resolution EM of Colloidal Nanocrystal Growth Using Graphene Liquid Cells. *Science* **2012**, *336*, 61–65.

(12) Wu, S.; Li, M.; Sun, Y. In Situ Synchrotron X-Ray Characterization Shining Light on the Nucleation and Growth Kinetics of Colloidal Nanoparticles. *Angew. Chemie. Int. Ed.* **2019**, *58*, 2–11.

(13) Ingham, B. X-Ray Scattering Characterisation of Nanoparticles. *Crystallogr. Rev.* **2015**, *21*, 229–303.

(14) Li, T.; Senesi, A. J.; Lee, B. Small Angle X‐ray Scattering for Nanoparticle Research. *Chem. Rev.* **2016**, *116*, 11128–11180.

(15) Staniuk, M.; Hirsch, O.; Kranzlin, N.; Bohlen, R.; Van Beek, W.; Abdala, P. M.; Koziej, D. Puzzling Mechanism behind a Simple Synthesis of Cobalt and Cobalt Oxide Nanoparticles: In Situ Synchrotron X-Ray Absorption and Diffraction Studies. *Chem. Mater.* **2014**, *26*, 2086–2094.

(16) Wu, L.; Lian, H.; Willis, J. J.; Goodman, E. D.; McKay, I. S.; Qin, J.; Tassone, C. J.; Cargnello, M. Tuning Precursor Reactivity toward Nanometer-Size Control in Palladium Nanoparticles Studied by in Situ Small Angle X-Ray Scattering. *Chem. Mater.* **2018**, *30*, 1127–1135.

(17) Abécassis, B.; Testard, F.; Spalla, O.; Barboux, P. Probing in Situ the Nucleation and Growth of Gold Nanoparticles by Small-Angle X-Ray Scattering. *Nano Lett.* **2007**, *7*, 1723–1727.

(18) Henkel, A.; Schubert, O.; Plech, A.; Sönnichsen, C. Growth Kinetic of a Rod-Shaped Metal Nanocrystal. *J. Phys. Chem. C* **2009**, *113*, 10390–10394.

(19) Polte, J.; Erler, R.; Thunemann, A.F.; Sokolov, S.; Ahner, T.T.; Rademann, K.; Emmerling, F.; Kraehnert, R. Nucleation and Growth of Gold Nanoparticles Studied via in Situ Small Angle X-Ray Scattering at Millisecond Time Resolution. *ACS Nano* **2010**, *4*, 1076–1082.

(20) Polte, J.; Ahner, T.T.; Delissen, F.; Sokolov, S.; Emmerling, F.; Thunemann, A.F.; Kraehnert, R. Mechanism of Gold Nanoparticle Formation in the Classical Citrate Synthesis Method Derived from Coupled in Situ XANES and SAXS Evaluation. *J. Am. Chem. Soc.* **2010**, *132*, 1296–1301.

(21) Neagu, D.; Tsekouras, G.; Miller, D. N.; Ménard, H.; Irvine, J. T. S. In Situ Growth of Nanoparticles through Control of Non-Stoichiometry. *Nat. Chem.* **2013**, *5*, 916–923.

(22) Shen, X.; Zhang, C.; Zhang, S.; Dai, S.; Zhang, G.; Ge, M.; Pan, Y.; Sharkey, S. M.; Graham, G. W.; Hunt, A.; et al. Deconvolution of Octahedral Pt_3Ni Nanoparticle Growth Pathway from in Situ Characterizations. *Nat. Commun.* **2018**, *9*, 4485.

(23) Peng, S.; Okasinski, J. S.; Almer, J. D.; Ren, Y.; Wang, L.; Yang, W.; Sun, Y. Real-Time Probing of the Synthesis of Colloidal Silver Nanocubes with Time-Resolved High-Energy Synchrotron X-Ray Diffraction. *J. Phys. Chem. C* **2012**, *116*, 11842–11847.

(24) Sun, Y.; Zuo, X.; Sankaranarayanan, S. K. R. S.; Peng, S.; Narayanan, B.; Kamath, G. Quantitative 3D Evolution of Colloidal Nanoparticle Oxidation in Solution. *Science* **2017**, *356*, 303–307.

(25) Sakamoto, N.; Harada, M.; Hashimoto, T. In Situ and Time-Resolved SAXS Studies of Pd Nanoparticle Formation in a Template of Block Copolymer Microdomain Structures. *Macromolecules* **2006**, *39*, 1116–1124.

(26) Takesue, M.; Tomura, T.; Yamada, M.; Hata, K.; Kuwamoto, S.; Yonezawa, T. Size of Elementary Clusters and Process Period in Silver Nanoparticle Formation. *J. Am. Chem. Soc.* **2011**, *133*, 14164–14167.

(27) Van Der Stam, W.; Rabouw, F. T.; Geuchies, J. J.; Berends, A. C.; Hinterding, S. O. M.; Geitenbeek, R. G.; Van Der Lit, J.; Prévost, S.; Petukhov, A. V.; De Mello Donega, C. In Situ Probing of Stack-Templated Growth of Ultrathin $Cu_{2-X}S$ Nanosheets. *Chem. Mater.* **2016**, *28*, 6381–6389.

(28) Cheong, S.; Watt, J.; Ingham, B.; Toney, M. F.; Tilley, R. D. In Situ and Ex Situ Studies of Platinum Nanocrystals: Growth and Evolution in Solution. *J. Am. Chem. Soc.* **2009**, *131*, 14590–14595.

(29) Chang, H.; Kim, B. H.; Jeong, H. Y.; Moon, J. H.; Park, M.; Shin, K.; Chae, S. I.; Lee, J.; Kang, T.; Choi, B. K.; Yang, J.; Bootharaju, M. S.; Song, H.; An, S.H.; Park, K. M.; Oh, J. Y.; Lee, H.; Kim, M.S.; Park, J.; Hyeon, T. Molecular-Level Understanding of Continuous Growth from Iron-Oxo Clusters to Iron Oxide Nanoparticles. *J. Am. Chem. Soc.* **2019**, *141*, 7037–7045.

(30) Chandra, K.; Rugg, B. K.; Ratner, M. A.; Wasielewski, M. R.; Odom, T. W. Detecting and Visualizing Reaction Intermediates of Anisotropic Nanoparticle Growth. *J. Am. Chem. Soc.* **2018**, *140*, 3219–3222.

(31) Ortiz, N.; Hammons, J. A.; Cheong, S.; Skrabalak, S. E. Monitoring Ligand-Mediated Growth and Aggregation of Metal Nanoparticles and Nanodendrites by In Situ Synchrotron Scattering Techniques. *ChemNanoMat* **2015**, *1*, 109–114.

(32) Yao, T.; Liu, S.; Sun, Z.; Li, Y.; He, S.; Cheng, H.; Xie, Y.; Liu, Q.; Jiang, Y.; Wu, Z.; Pan, Z.; Yan, W.; Wei, S. Probing Nucleation Pathways for Morphological Manipulation of Platinum Nanocrystals. *J. Am. Chem. Soc.* **2012**, *134*, 9410–9416.

(33) St. John, S.; Hu, N.; Schaefer, D. W.; Angelopoulos, A. P. Time-Resolved, in Situ, Small- and Wide-Angle X-Ray Scattering to Monitor Pt Nanoparticle Structure Evolution Stabilized by Adsorbed SnCl3- Ligands during Synthesis. *J. Phys. Chem. C* **2013**, *117*, 7924–7933.

(34) Jensen, K. M. Ø.; Christensen, M.; Juhas, P.; Tyrsted, C.; Bøjesen, E. D.; Lock, N.; Billinge, S. J. L.; Iversen, B. B. Revealing the Mechanisms behind SnO2 Nanoparticle Formation and Growth during Hydrothermal Synthesis: An in Situ Total Scattering Study. *J. Am. Chem. Soc.* **2012**, 134, 6785–6792.

(35) Gromova, M.; Lefranç, A.; Vaure, L.; Agnese, F.; Aldakov, D.; Maurice, A.; Djurado, D.; Lebrun, C.; De Geyer, A.; Schülli, T. U.; Pouget, S.; Reiss, P. Growth Mechanism and

Surface State of CuInS2 Nanocrystals Synthesized with Dodecanethiol. *J. Am. Chem. Soc* **2017**, *139*, 15748–15759.

(36) Krishna, K.S.; Navin, C. V.; Biswas, S.; Singh, V.; Ham, K.; Bovenkamp, G. L.; Theegala, C. S.; Miller, J. T.; Spivey, J. J.; Kumar, C. S. S. R. Millifluidics for Time-Resolved Mapping of the Growth of Gold Nanostructures. *J. Am. Chem. Soc.* **2013**, *135*, 5450–5456.

(37) Abécassis, B.; Bouet, C.; Garnero, C.; Constantin, D.; Lequeux, N.; Ithurria, S.; Dubertret, B.; Pauw, B. R.; Pontoni, D. Real-Time in Situ Probing of High-Temperature Quantum Dots Solution Synthesis. *Nano Lett.* **2015**, *15*, 2620–2626.

(38) Wu, L.; Willis, J. J.; McKay, I. S.; Diroll, B. T.; Qin, J.; Cargnello, M.; Tassone, C. J. High-Temperature Crystallization of Nanocrystals into Three-Dimensional Superlattices. *Nature* **2017**, *548*, 197–201.

(39) Yao, T.; Sun, Z.; Li, Y.; Pan, Z.; Wei, H.; Xie, Y.; Nomura, M.; Niwa, Y.; Yan, W.; Wu, Z.; Jiang, Y.; Liu, Q.; Wei, S. Insights into Initial Kinetic Nucleation of Gold Nanocrystals. *J. Am. Chem. Soc.* **2010**, *132*, 7696–7701.

(40) Karim, A. M.; Al Hasan, N.; Ivanov, S.; Siefert, S.; Kelly, R. T.; Hallfors, N. G.; Benavidez, A.; Kovarik, L.; Jenkins, A.; Winans, R. E.; Datye, A.K. Synthesis of 1 nm Pd Nanoparticles in a Microfluidic Reactor: Insights from in Situ X-Ray Absorption Fine Structure Spectroscopy and Small-Angle X-Ray Scattering. *J. Phys. Chem. C* **2015**, *119*, 13257–13267.

(41) Mozaffari, S.; Li, W.; Thompson, C.; Ivanov, S.; Seifert, S.; Lee, B.; Kovarik, L.; Karim, A. M. Colloidal Nanoparticle Size Control: Experimental and Kinetic Modeling Investigation of the Ligand-Metal Binding Role in Controlling the Nucleation and Growth Kinetics. *Nanoscale* **2017**, *9*, 13772–13785

(42) Manocchi, A. K.; Seifert, S.; Lee, B.; Yi, H. In Situ Small-Angle X-Ray Scattering Analysis of Palladium Nanoparticle Growth on Tobacco Mosaic Virus Nanotemplates. *Langmuir* **2011**, *27*, 7052–7058.

(43) Cormary, B.; Li, T.; Liakakos, N.; Peres, L.; Fazzini, P. F.; Blon, T.; Respaud, M.; Kropf, A. J.; Chaudret, B.; Miller, J. T.; Mader, E.A.; Soulantica, K. Concerted Growth and Ordering of Cobalt Nanorod Arrays as Revealed by Tandem in Situ SAXS-XAS Studies. *J. Am. Chem. Soc.* **2016**, 138, 8422–8431.

(44) Sun, Y.; Ren, Y. In Situ Synchrotron X-Ray Techniques for Real-Time Probing of Colloidal Nanoparticle Synthesis. *Part. Part. Syst. Charact.* **2013**, 30, 399–419.

(45) Lassenberger, A.; Grünewald, T. A.; Van Oostrum, P. D. J.; Rennhofer, H.; Amenitsch, H.; Zirbs, R.; Lichtenegger, H. C.; Reimhult, E. Monodisperse Iron Oxide Nanoparticles by Thermal Decomposition: Elucidating Particle Formation by Second-Resolved in Situ Small-Angle X-Ray Scattering. *Chem. Mater.* **2017**, *29*, 4511–4522.

(46) Gawande, M. B.; Goswami, A.; Felpin, F. O.-X.; Asefa, T.; Huang, X.; Silva, R.; Zou, X.; Zboril, R.; Varma, R. S. Cu and Cu-Based Nanoparticles: Synthesis and Applications in Catalysis. *Chem. Rev.* **2016**, 216, 372280–3811.

(47) Ma, M.; Djanashvili, K.; Smith, W. A. Controllable Hydrocarbon Formation from the Electrochemical Reduction of CO2 over Cu Nanowire Arrays. *Angew. Chemie. Int. Ed.* **2016**, *55*, 6680–6684.

(48) Reske, R.; Mistry, H.; Behafarid, F.; Roldan Cuenya, B.; Strasser, P. Particle Size Effects in the Catalytic Electroreduction of CO_2 on Cu Nanoparticles. *J. Am. Chem. Soc.* **2014**, *136*, 6978–6986.

(49) Iyengar, P.; Huang, J.; De Gregorio, G. L.; Gadiyar, C.; Buonsanti, R. Size Dependent Selectivity of Cu Nano-Octahedra Catalysts for the Electrochemical Reduction of CO_2 to CH_4. *Chem. Commun.* **2019**, *55*, 8796-8799

(50) Suen, N.-T.; Kong, Z.-R.; Hsu, C.-S.; Chen, H.-C.; Tung, C.-W.; Lu, Y.-R.; Dong, C.-L.; Shen, C.-C.; Chung, J.-C.; Chen, H. M. Morphology Manipulation of Copper Nanocrystals and Product Selectivity in the Electrocatalytic Reduction of Carbon Dioxide. *ACS Catal.* **2019**, *9*, 5217–5222.

(51) Li, Y.; Cui, F.; Ross, M. B.; Kim, D.; Sun, Y.; Yang, P. Structure-Sensitive CO_2 Electroreduction to Hydrocarbons on Ultrathin 5-Fold Twinned Copper Nanowires. *Nano Lett.* **2017**, *17*, 1312–1317.

(52) Loiudice, A.; Lobaccaro, P.; Kamali, E. A.; Thao, T.; Huang, B. H.; Ager, J. W.; Buonsanti, R. Tailoring Copper Nanocrystals towards C2 Products in Electrochemical CO_2 Reduction. *Angew. Chemie. Int. Ed.* **2016**, 55, 5789–5792.

(53) Coughlan, C.; Ibáñez, M.; Dobrozhan, O.; Singh, A.; Cabot, A.; Ryan, K. M. Compound Copper Chalcogenide Nanocrystals. *Chem. Rev.* **2017**, *117*, 5865–6109.

(54) Mantella, V.; Ninova, S.; Saris, S.; Loiudice, A.; Aschauer, U.; Buonsanti, R. Synthesis and Size-Dependent Optical Properties of Intermediate Band Gap Cu_3VS_4 Nanocrystals. *Chem. Mater.* **2019**, *31*, 532–540.

(55) Gadiyar, C.; Strach, M.; Schouwink, P.; Loiudice, A.; Buonsanti, R. Chemical Transformations at the Nanoscale: Nanocrystal-Seeded Synthesis of β-Cu2V2O7 with Enhanced Photoconversion Efficiencies. *Chem. Sci.* **2018**, *9*, 5658–5665.

(56) Shin, H. C.; Choi, S. C.; Jung, K. D.; Han, S. H. Mechanism of M Ferrites (M = Cu and Ni) in the CO2 Decomposition Reaction. *Chem. Mater.* **2001**, *13*, 1238–1242.

(57) Jin, M.; He, G.; Zhang, H.; Zeng, J.; Xie, Z.; Xia, Y. Shape-Controlled Synthesis of Copper Nanocrystals in an Aqueous Solution with Glucose as a Reducing Agent and Hexadecylamine as a Capping Agent. *Angew. Chemie. Int. Ed.* **2011**, *50*, 10560–10564.

(58) Lyu, Z.; Xie, M.; Gilroy, K. D.; Hood, Z. D.; Zhao, M.; Zhou, S.; Liu, J.; Xia, Y. A Rationally Designed Route to the One-Pot Synthesis of Right Bipyramidal Nanocrystals of Copper. *Chem. Mater.* **2018**, *30*, 6469–6477.

(59) Hung, L. L.; Tsung, C. K.; Huang, W.; Yang, P. Room-Temperature Formation of Hollow Cu_2O Nanoparticles. *Adv. Mater.* **2010**, *22* , 1910–1914.

(60) Guo, H.; Chen, Y.; Cortie, M. B.; Liu, X.; Xie, Q.; Wang, X.; Peng, D. L. Shape-Selective Formation of Monodisperse Copper Nanospheres and Nanocubes via Disproportionation Reaction Route and Their Optical Properties. *J. Phys. Chem. C* **2014**, *118*, 9801–9808.

(61) Ye, E.; Zhang, S. Y.; Liu, S.; Han, M. Y. Disproportionation for Growing Copper Nanowires and Their Controlled Self-Assembly Facilitated by Ligand Exchange. *Chem. - A Eur. J.* **2011**, *17*, 3074–3077.

(62) Jana, N. R.; Peng, X. Single-Phase and Gram-Scale Routes toward Nearly Monodisperse Au and Other Noble Metal Nanocrystals. *J. Am. Chem. Soc*. **2003**, *125*, 14280-14281.

(63) Weare, W. W.; Reed, S. M.; Warner, M. G.; Hutchison, J. E. Improved Synthesis of Small ($d_{CORE} \approx 1.5$ nm) Phosphine-Stabilized Gold Nanoparticles. *J. Am. Chem. Soc*. **2000**, *122*, 12890-12891.

(64) Wang, Z. L. Transmission Electron Microscopy of Shape-Controlled Nanocrystals and Their Assemblies, *J. Phys. Chem. B* **2000**, *104*, 1153-1175.

(65) Nishimura, S.; Takagaki, A.; Maenosono, S.; Ebitani, K. In Situ Time-Resolved XAFS Study on the Formation Mechanism of Cu Nanoparticles Using Poly(N-vinyl-2-pyrrolidone) as a Capping Agent. *Langmuir*, **2010**, *26*, 4473-4479.